Progress in Additive Manufacturing
https://doi.org/10.1007/s40964-024-00689-8

FULL RESEARCH ARTICLE

Thermal history transfer from complex components to representative test specimens in laser powder bed fusion

Gunther Mohr[1] · Mohsin Ali Chaudry[1] · Nils Scheuschner[1] · Sergio Blasón González[1] · Mauro Madia[1] · Kai Hilgenberg[1]

Received: 3 January 2024 / Accepted: 27 May 2024

Abstract
Additively manufactured components are characterized by heterogeneous mechanical properties due to variations of the microstructure, flaws and residual stresses resulting from the inhomogeneous fabrication process. The large number of influencing factors poses a further challenge in understanding the correlation between material properties, process parameters and component geometry. Therefore, the qualification of components based on witness specimens produced within the same job is questionable. This work aims to present a new strategy for the characterization of PBF-LB/M components based on representative specimens. The key assumption is the feasibility of a transfer of the thermal history from a component to a specimen. It is assumed that similar material properties are determined for components and specimens produced adopting a similar thermal history. After the definition of a region of interest in the component, a combination of thermal analyses by means of finite elements and in-situ experimental determination of the thermal history through infrared thermography is used to produce test coupons with a similar thermal history. The effectiveness of the procedure is demonstrated on a pressure vessel for applications in the chemical industry.

Keywords Powder Bed Fusion (PBF) · Laser Beam Melting (LBM) · Representative specimens · Finite element method · Process simulation · Process monitoring · Thermal history · Inter layer time

1 Introduction

Additive manufacturing (AM) technologies have matured from systems for prototyping applications to manufacturing systems with greater industrial relevance for small and medium sized serial production. The laser powder bed fusion process (PBF-LB/M) is the most widespread technology among the distinct AM technologies for the production of metallic parts. Despite the growing field of specific PBF-LB/M manufacturing systems and several industrial applications, doubts against the use of this manufacturing technology for the production of safety-relevant components subjected to fatigue loading are still raised [1, 2]. The main concerns are caused by the uncertainty about the homogeneity of the process results due to the high number of influencing factors which increase the risk of process instability and resulting inhomogeneity of properties within one built part or in comparison between several built parts from one or more built processes [3, 4]. The layer-wise nature of the PBF-LB/M process and the large total length of the melting tracks of a built part contribute to this uncertainty as they both increase the risk of generating flaws or irregularities into the final product. Therefore, a strong focus is set on the development of material specific and machine specific processing parameters which can be used to produce considerably dense parts with acceptable mechanical properties [5]. At the same time, many other influencing factors such as raw material properties, or shielding gas-flow conditions are preferably kept as constant as possible to get reliable and reproducible manufacturing results. This is a widely accepted strategy for the development of process parameters based on small laboratory specimens. However, their applicability for the manufacturing of complex components is not given in any case [6]. The understanding of flaw formation and causes of microstructure inhomogeneity in components has been identified as critical [7].

✉ Gunther Mohr
gunther.mohr@bam.de

[1] Bundesanstalt für Materialforschung und -prüfung, Unter den Eichen 87, 12205 Berlin, Germany

Published online: 09 June 2024

The component's geometry itself is an additional influencing factor which varies according to the design resulting in variations of the thermal history [8–10]. This inherently complicates the desire of having constant and comparable conditions in all build processes. Complex geometries lead to strong variations of process conditions during the fabrication of the part. The relationship between the manufacturing process, the geometrical features and resulting properties is still a matter of investigation and a deeper knowledge on this matter is highly desired [11]. In fact, the geometrical characteristics can have various influences on the final properties [2, 12].

On the one hand, anisotropy as a result of build angle variation and directional solidification conditions is one of the obvious issues which have to be considered [13]. This is usually already taken into account in the determination of material properties by manufacturing test specimens under various build angles, usually 0°, 45°, and 90° with respect to the build plate [14–16]. Furthermore, process-related restrictions may limit the manufacturability of a specific design. Principle rules of design for additive manufacturing (DfAM) approaches may help to solve such issues [17].

On the other hand, the thermal conditions of the part during manufacturing are also influenced by the geometry. Not only the conditions of heat conduction through the growing part are affected by the geometry but also its variable cross-section areas, the number of parts per build process, and the number of laser sources involved in the manufacturing process also determine the inter layer time (ILT) and therefore the cooling phases between subsequent melting of layers [18, 19]. The combination of both can lead to changes of the thermal preconditions for the melting process, e.g., by the built up of significant heat accumulation [20, 21]. Heat accumulation has been identified as a major issue in PBF-LB/M by several authors [9, 22, 23]. Mohr et al. showed in their investigation of cuboid specimens with varying sizes of the geometrical connection to the build plate significant process intrinsic heat accumulation with temperatures up to 900 °C [6]. They also discussed the effect of elevated intrinsic preheating temperatures on resulting occurrence of defects and grain sizes, as well as the size of the cellular sub-structure in the case of PBF-LB/M fabrication using 316L [24]. Koenis et al. [9] showed a significant reduction in failure strain in overheated Ti6Al4V specimens, while having only a minor increase in UTS and yield strength. They also noticed a significant oxygen pick up in regions of significant heat accumulation, similar to other work by Pauzon et al. [25]. The geometric susceptibility to heat accumulation during PBF-LB/M needs to be considered when evaluating the process results [12, 26].

Therefore, it is questioned whether and to which extent material properties determined on fabricated test coupons can be used for the characterization and qualification of components with different volume and geometry and different build-process conditions. A simply shaped test coupon usually faces another thermal history than a complexly shaped real part, which may affect the resulting properties and impede a direct comparison. Because of this uncertainty, costly preparation of specimens directly from the real components is necessary which comes along with the destruction of the expensive parts. Zerbst et al. [1] pointed out this problem in their comprehensive review on damage tolerant design of additively manufactured metallic components and emphasized the special necessity of developing specimens that match the properties of the component. In their comprehensive review on repeatability and reliability of AM, Venturi and Taylor recently underlined that correlations between witness coupons and components are not fully developed yet [2]. They also expressed the desire for a geometry-based methodology for witness coupons. A more refined methodology could help to reduce the testing efforts at component-scale, and could meet the desire of the industry and regulatory agencies to still rely on physical validations [2].

This work aims to introduce a new paradigm for the determination of material properties in PBF-LB/M parts based on so-called representative specimens. The fundamental underlying idea is the assumption of thermal history similarity between component and specimen [27]. It is expected that components undergoing similar temperature histories are likely to develop similar microstructures and eventually show similar mechanical properties. The interdependency of microstructure on the thermal history was shown by Pantawane et al. [28]. In their work, they correlated the evolution of microstructure based on temperature profiles for PBF-LB/M manufacturing of Ti6Al4V. Similarly, Kelly et al. [29] developed a microstructural-evolution map based on the thermal mode for laser metal deposition of Ti6Al4V. Deviations of the initial surface temperature as a result of heat accumulation during the manufacturing process may lead to differences in the resulting microstructure as shown for the PBF-LB/M based manufacturing of 316L [24]. The thermal history of a region of interest (ROI) of a real part component should be similar to the thermal history of a specimen if that specimen is supposed to represent the component's properties of that ROI. It is also assumed that similar thermal histories generate similar defect types, which are even more important than the microstructure concerning the fatigue life. Correlations between thermal histories and defect occurrence have already been described in the literature [6, 30]. Furthermore, it is expected that residual stresses might have a major influence on the determination of fatigue life. However, the authors are aware that, unlike microstructure and inherent flaws, the build-up of residual stresses is highly dependent on the geometrical constraint in the component, which cannot be fully reproduced within a simply shaped representative specimen. However, this issue

can be evaluated as an issue of a secondary order, when applying appropriate stress-relieving heat treatments.

The thermal history is the temporal change of the temperature field T(x,y,z) during the build-up process. Riensche et al. identified this spatiotemporal temperature distribution as a major cause for flaw formation [23]. The temperature field can be divided into two characteristic regions, a near-temperature field and a far-temperature field [31]. The near-temperature field comprises the direct vicinity of the laser beam irradiation and thus the melt pool and the directly surrounding region, which is characterized by a steep thermal gradient (partial derivatives dT/dx, dT/dy, dT/dz as well as dT/dt). It can be assumed that this temperature field is mainly determined by the energy input, i.e., by the process parameters laser power and scan speed and the overall absorptivity of the material. The temperature far-field, on the other hand, is characterized by much lower temperature gradients in space and time and comprises the entire component built up so far. Its characteristics are influenced in particular by the geometry and the possible heat dissipation into the already built-up geometry or into the build plate. The ILT, which is directly dependent on the exposed area and thus the geometry, has in addition proven to be a particular influencing factor [6]. The temperature far field determines the temperature distribution of the top layer after exposure and decay of the temperature peak of the laser energy input. This surface temperature distribution acts as an intrinsic preheating temperature for the subsequent exposure. In this study, this intrinsic preheating temperature is considered as the measure of comparability among thermal histories. The practical implementation of the concept includes the use of FEM-based macroscale thermal simulations, the adoption of the specimen manufacturing process based on the adjustment of the inter layer times and a validation by use of a in-situ measurement of the thermal field by means of a calibrated infrared camera. The applicability of the concept is demonstrated considering a pressure vessel geometry from the chemical industry as large scale PBF-LB/M component.

Recently, a similar approach has been discussed by Chandrasekar et al. [11]. They used thermal history similarity as a comparison criterion to assess critical regions in components based on data setsdetermined on test specimens beforehand. They demonstrated correlations of thermal signatures with grain sizes and microstructure variation within a part produced by 316L, which also demonstrates the validity of the thermal history similarity approach. Their concept requires a huge data library with stored thermal-signature-microstructure-correlations, and it comes with the risk that the boundary conditions of the process used for the acquisition of the reference data sets differ from that of the component to be assessed later on (e.g., different powder batch, different filter condition etc.). The novelty of the concept introduced in this manuscript is the direct transferability of the thermal history from the ROI of a component to a test specimen, which can be built under the same conditions directly after the component build process and taken for mechanical testing.

2 Materials and methods

The transferability of the thermal history of a critical volume within a real part geometry to a simply shaped test specimen involves several steps. They are summarized in the flow chart in Fig. 1. Some parts of the section materials and methods already require a partial anticipation of results, presented in the section on results and discussion. Further essential information of the component design and the manufacturing conditions are given in Sects. 2.1 and 2.2.1, respectively.

2.1 Geometry of the demonstrator

A pressure vessel for applications in the chemical industry was taken as a demonstrator to be manufactured by PBF-LB/M. The geometry, which was provided by the company BASF SE (Ludwigshafen, Germany), represents a compromise between fabrication requirements and the need to extract specimens for fatigue testing. The total height of the vessel was 220 mm, and the outer diameter was 147.75 mm. Figure 2 depicts a photograph of the manufactured component on the build plate and a vertical cut through the 3D-CAD-model. It can be seen that the component was double walled. The outer wall had a constant thickness of 2 mm, whereas the inner wall varied in its thickness. The inner wall comprised three different regions: A, B and C, as depicted in Fig. 2. Region C was designed with a wall thickness of 15 mm, whereas region B and region A were designed with a wall thickness of 11 mm. The cone was designed on purpose to induce a strong variation of the ILT and to investigate the effect of the overhanging region.

2.2 Experimental work

2.2.1 PBF-LB/M machine, processing parameters and feedstock material

All experimental work was executed on a PBF-LB/M machine of type SLM280HL (SLM Solutions Group AG, Lübeck, Germany), equipped with a 1070 nm cw laser with laser power of up to 400 W and a spotsize of approx. 80 µm. Argon was used as shielding gas. The material used for the manufacturing was stainless steel 316L. As feedstock material spherical powder with a particle fraction of 15 µm to 53 µm was used. The powder was delivered by VDM Metals International GmbH, Werdohl, Germany. The component was built on top of a cylinder of full volume support of 4 mm thickness, which was manufactured

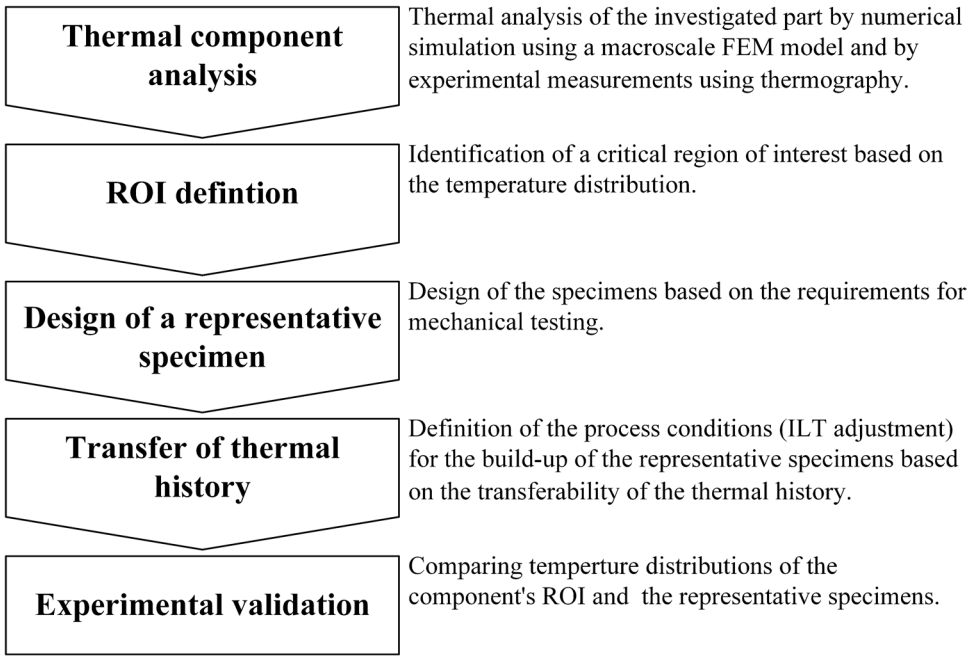

Fig. 1 Process workflow to transfer the thermal history of a critical volume in a component to simply shaped test specimens

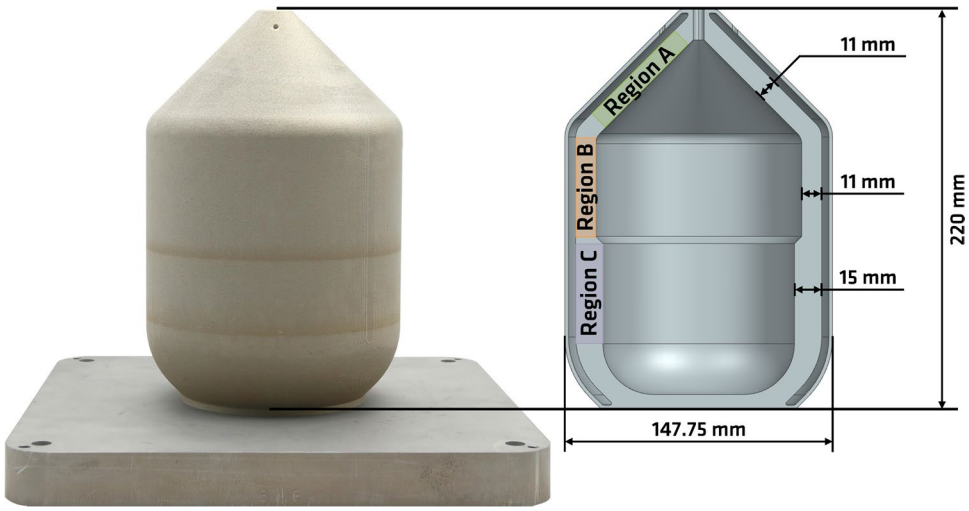

Fig. 2 Pressure vessel produced by means of PBF-LB/M (left) and cross-section of CAD geometry (right)

using the same process parameters as for the component. These were: laser power of 275 W, scanning velocity of 700 mm s^{-1}, hatch distance of 0.12 mm and a layer thickness of 0.05 mm. A base plate preheating of 100 °C was used. The bulk was manufactured without using any contour scans. A stripe scanning strategy with a stripe length of 10 mm was used. The scanning pattern rotated by 30° after each layer. No minimal exposure time was used. Therefore, the ILT of each layer was directly determined by the area of the cross sections to be exposed throughout the course of the 4480 layers. The variation of the ILT over the build height is depicted in Fig. 3. The specific values were obtained from the log file of the PBF-LB/M machine.

2.2.2 Temperature measurement by in-situ thermal IR monitoring

The manufacturing processes were monitored using an off-axis mounted mid-wave infrared (MWIR) camera of type ImageIR8300 (Infratech GmbH, Dresden, Germany). The camera was installed on top of the PBF-LB/M machine and had optical access via a sapphire window in the ceiling of the build chamber. The optical path within the build chamber was tilted by two gold-coated mirrors to have an almost perpendicular view on the build plate and to manually adjust the position of the field of view during the preparation of the build process. The same camera was also used in previous

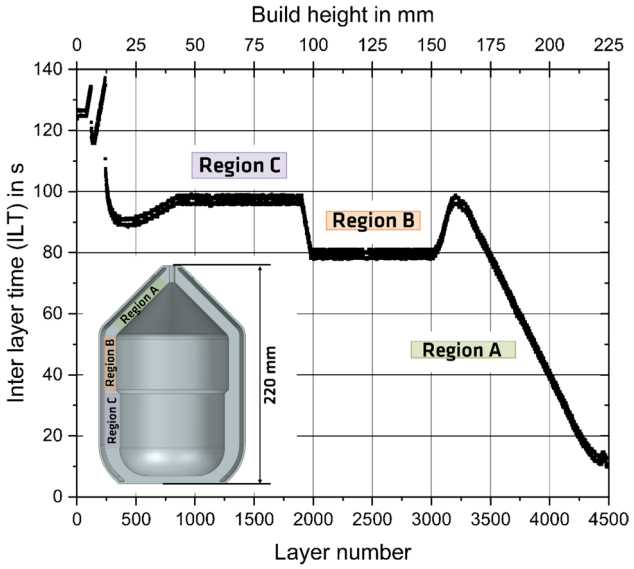

Fig. 3 Variation of inter layer time throughout the build-up of the component. The additional volume support of 4 mm height is not included in the illustration of the demonstrator

studies in the same setup, see [20, 24] for more details. The data were sampled at a frame rate of 60 Hz, and the spatial resolution of the camera was approx. 420 µm/pixel. For the measurements, a calibration range valid for black body temperatures of 125–300 °C was used with a resulting integration time of 27 µs. To correct for the influence of the emissivity onto the apparent temperatures of the 316L powder layers and for PBF-LB/M/316L surfaces an emissivity value of 0.33 was used which was determined in a previous experimental study using the same camera setup and PBF-LB/M machine [32]. The thermal data extraction was executed in the condition of a surface freshly recoated by a powder layer right before the next exposition of the part. This temperature was referred to as the intrinsic preheating temperature T_0 (layer) of the part. These preheating temperature values of the growing built part were taken for the evaluation and comparison of the thermal history.

For the extraction of thermal data, aMatlab routine was used. A squared region of 10 mm by 10 mm was chosen as the ROI for the signal extraction. This was applied to the lower part of the demonstrator at the centre of the inner wall and later also to the representative specimens (introduced in Sect. 2.5) In the upper part of the demonstrator (region A and region B in Fig. 2), the ROI was decreased to an area of 5 mm by 5 mm. The average values of these selected regions were taken for the surface temperature determination. Due to the rotation of the scanning vectors and the variation of the starting point of the laser exposition, the sequence of laser scanning varied from layer to layer. Consequently, the location specific ILT can vary, which influences the local surface temperature for a given region from one layer to another. To diminish these effects in the measurements and for the sake of a better comparison of the measured temperatures with the macroscale thermal simulation results, the determination of surface temperature values was only conducted for layers which were scanned with the same angle of the scanning pattern. The thermal data extraction was conducted for several layers of the demonstrator as well as of the representative specimen.

2.3 Transient thermal analysis

The finite element method (FEM) was used for the numerical prediction of the thermal field during PBF-LB/M based part production to gain intrinsic preheating temperatures for quantitative comparison with experimental data. In the following subsections the methodology, the applied heat source and the assumptions used for the material parameters are briefly described, followed by the decription of the temperature prediction by numerical modeling.

2.3.1 Methodology

The information about the temperature evolution was of primary interest in this study, as the fabrication of the representative specimens is based on the similarity of the thermal history. Therefore, a pure transient thermal analysis was carried out, neglecting any coupling to the mechanical field. For the analysis, the thermal field at the end of the scanning of each layer was needed. At this instant, the temperature profile is nearly homogenized over the layer and a steep thermal gradient is not observed. Therefore, it was sufficient to use a macroscale model, where the heat source was applied over the entire layer at once. The general validity of such an macroscale modeling approach have been shown at simple geometries in a previous work [33]. The temperature field was calculated according to the general heat Eq. (1):

$$\rho c \frac{\partial T}{\partial t} = k\left(\frac{\partial^2 T}{\partial x^2} + \frac{\partial^2 T}{\partial y^2} + \frac{\partial^2 T}{\partial z^2}\right) + Q_v, \tag{1}$$

where ρ represents density, c the specific heat capacity, k the thermal conductivity, T the temperature and Q_v is the energy rate per unit volume. For the solution of the heat equation for any given body, the body is discretized into a finite number of elements and the Eq. (1) is transformed into the weak form, which results in algebraic equations. These equations are then solved to determine the unknown temperature field, see [34] for further details. For the solution of the initial boundary value problem, the preheating temperature of the current layer represents the initial temperature T_0. In addition, Eq. (2) represents the convection-boundary condition, where h is the convection coefficient and T_∞ represents the ambient temperature. For the FEM model, the

convection-boundary condition was applied to the current top surface of each layer of the part. The boundary conditions are described in more detail for each of the test cases in the respective sections of this manuscript.

$$q = h\left(T - T_{\infty}\right). \tag{2}$$

2.3.2 Heat source

As a macroscale model was used for the numerical analysis, the definition of the heat source (Q_v) becomes important. The heat source is derived based on the principle of energy equivalence. The equivalent energy is calculated according to the following equation:

$$E_{\mathrm{eq}} = \eta P t_{\mathrm{scan}} \tag{3}$$

with

$$t_{\mathrm{scan}} = \frac{\mathrm{Area}}{v_{\mathrm{l}}\, h_{\mathrm{d}}}. \tag{4}$$

In Eq. (3), η represents the absorption coefficient, P the laser power and t_{scan} the time needed to expose the cross-section area of a layer by the laser. The scanning time t_{scan}, defined in Eq. (4), was calculated from the cross-section area of a layer, the scanning velocity v_{l}, and the hatch distance h_{d} as the distance between adjacent scanning vectors. For simplification, any time contribution resulting from sky writing and jump vectors is neglected. The absorption coefficient is an important parameter, which defines the fraction of laser energy absorbed by the material. The absorption coefficient can vary significantly depending on the prevalent welding mode [35, 36]. The material specific absorption coefficient depends mainly on the energy input per unit length defined by the scanning velocity and the laser power [37]. From previous work [18] it is known that deep-penetration mode welding is the prevalent welding mode when using the given set of process parameters at the given machine for stainless steel 316L. Hence, an estimated value of 0.75 was chosen as absorption coefficient η. It was chosen based on the results of Trapp et al. [36] for deep-penetration mode welding.

Using the total energy calculated in Eq. (3), the volumetric heat source is calculated from Eq. (5).

$$Q_{\mathrm{vol}} = \frac{E_{\mathrm{eq}}}{t_{\mathrm{mp}} V_{\mathrm{mp}}}. \tag{5}$$

In Eq. (5), Q_{vol} represents the volumetric heat source, E_{eq} was calculated from Eq. (3), V_{mp} is the volume of layers to which the heat source is applied, and t_{mp} is the time for which the volumetric heat source is applied. The exposition time t_{mp}, was calculated from the scanning velocity and the estimated length of the melt pool represented by the edge length surrounded by the melting isotherm.

$$t_{\mathrm{mp}} = \frac{\text{edge length}}{v_{\mathrm{l}}}. \tag{6}$$

This was described and used by Seidel and Zäh [38] for transient thermal simulation. The edge length used in this study was based on an approximation presented by Khan et al. [39], who used the same material and processing parameter conditions. For simplification, the edge length was applied as a constant for the entire part simulation, although different levels of heat accumulation were to be expected, which actually might lead to variations of this value. This simplification led to a constant value of the exposition time of 0.001 s.

It is important to notice, that the volume V_{mp} represents the volume of layers to which the heat source is applied and which in turn gets molten. Therefore, it is improper to consider only the current topmost layer. In addition to the current topmost layer, several previously already solidified layers also get molten due to the deep-penetration mode [40]. Considering this observation, it was approximated that the heat source acts on four successive layers and the volume was chosen appropriately.

2.3.3 Material parameters

For the simulation, the thermophysical properties of the stainless austenitic steel 316L were considered in two distinct conditions, namely as powder and as solid bulk as discussed in previous work [33]. Initially, each layer is in powder condition and the material properties of a 316L powder layer are considered, which significantly vary from the material properties of solid bulk condition in terms of heat conductivity and apparent density. The powder geometry was not modeled in the FEM model but it was assumed as a continuum with appropriate homogenized properties. Later, the powder layer is exposed to the laser, gets molten and eventually solidifies. After the transition from loose powder to coherent bulk material, the material properties of solid 316L stainless steel were considered. In addition, the temperature dependency of the distinct material properties was also considered in the calculation and taken from mills [41]. The thermal conductivity of the powder deviates strongly from the thermal conductivity of the solid bulk material due to point contact of the powder particles. The calculation of thermal conductivity of the powder was conducted according to the work of Sih and Barlow [42]. The resulting thermal conductivity of the powder varied from 0.35 to 0.4 W m^{-1} K^{-1} for room temperature and solidus temperature, respectively. The resulting material properties

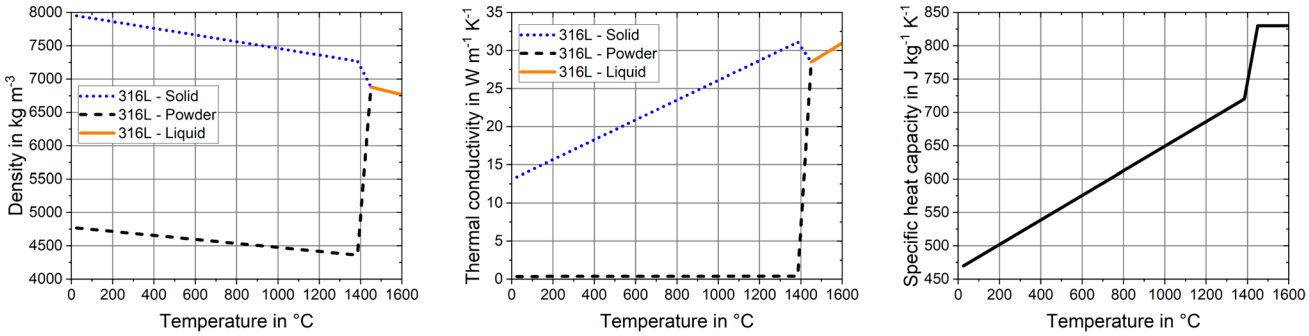

Fig. 4 Variation of density, thermal conductivity, and specific heat capacity with the temperature as used for the simulations, cf. [33]

are displayed in Fig. 4. These values were implemented in the temperature dependent numerical modeling.

2.3.4 Temperature prediction by numerical modeling

For the FEM-based simulation, the software Ansys Release 2019R3 was used. The geometry of the demonstrator (pressure vessel, described in Sect. 2.1) was surrounded by a bounding box with dimensions of 186 mm × 186 mm × 220 mm. The volume of this bounding box which did not belong to the volume of the demonstrator was treated as powder material with the appropriate powder material properties. The volume of the demonstrator was simulated as solid bulk material after laser exposition. It is important to notice, that the modeling of the powder surrounding the demonstrator was an essential point to ensure that heat dissipation was correctly modeled.

The whole model was partitioned into layers and then meshed with tetrahedral elements. The model comprised 2,503,930 elements. Therefore, a lumping strategy was implemented to ensure computational efficiency. Four layers were lumped together, and the heat source was applied to these layers simultaneously. Element birth–death technique was used for the simulation, where only elements were activated which were exposed to the laser radiation.

The following initial boundary conditions were applied: The bottom plate was kept at 100 °C, which comes from the platform preheating. The ambient temperature was assumed to be at 35 °C which is a usual value during the production of parts in the machine used for the experiments. Convection boundary condition was applied for every newly deposited layer. An estimated value of the convection coefficient of 0.06 W m^{-2} K^{-1} was used. This comparatively low value was chosen via calibration and mitigates errors resulting from simplifications made of the macroscopic modeling approach. The outer surfaces of the powder filled bounding box were taken as boundary with adiabatic conditions.

The heat source was applied to the respective cross sections of the component only and not to the surrounding powder. The simulation was conducted using the PBF-LB/M processing parameters presented in Sect. 2.2.1 and the heat source introduced in Sect. 2.3.2. In addition to the exposition phase, which represents the phase of energy intake, the PBF-LB/M component also underwent a cooling phase. Each lump of layers in the simulation underwent cooling for the duration calculated from the ILT of the topmost layer of each lump. Due to varying cross-sections of the vessel, the ILT was not constant but varied along the height of the vessel, as shown in Fig. 3.

The same procedure was used for the thermal analysis of the representative specimens. The only differences were the geometrical details (shape, dimensions) of the specimens and the bounding box. The bounding box had a size of 117 × 40 80 mm^3. The specimens are described in Sect. 2.4. The FEM model was meshed with 130,144 hexahedral elements. As in the case of the component, convection-boundary conditions were applied to the top of each layer. Since the computational effort of the simulation of the specimen was not significant, the lumping strategy was not used in this case and each layer was modeled with a thickness of 50 µm. The ILT used for the simulation was also not constant. Instead, it was purposely varied over the build height and thereby used as an active parameter influencing the thermal history. This strategy and the specific ILT values are presented in Sect. 2.4.3.

2.4 Design of the representative specimen

The intrinsic preheating temperature of a component's surface prior to laser exposition can be considered as an initial key value of the thermal history. The similarity criterion can therefore be applied to this temperature value, which is a measurable physical value in of macro scale thermal simulations.

The procedure of the design of a representative specimen followed three steps which are explained in the following subsections:

1. Determination of the thermal history of the demonstrator and definition of the ROI,
2. Definition of the geometry of the representative specimen, and
3. Development of a strategy to transfer the thermal history of the ROI to the representative specimen.

2.4.1 Determination of the thermal history of the demonstrator and definition of the ROI

The first step, the determination of the thermal history of a real component focusing on the part surface temperature, can be executed by thermal modeling or by experimental work. In this study, both strategies were followed, as the experimental work was directly used for the validation of the thermal modeling. Some of the results must be anticipated in this section already, as the definition of the ROI in the demonstrator is based on the results of the thermal analysis. The ROI of the component was chosen based on the region with the highest heat accumulation during the manufacturing process since the main objective was to perform rigorous investigation for the region which has potentially the highest presence of defects or microstructural deviations. The chosen process parameters have shown slight shifts of the processing window to a more unstable melting process inducing keyhole porosity when faced with elevated preheating temperatures in previous work [6, 18]. In addition, an increase in grain size and a decrease in hardness was observed in regions with higher heat accumulation. In the case of the specific pressure vessel, the highest heat accumulation was observed in the cone (region A, Fig. 2). Hence, the cone (region A) was chosen as ROI, for which representative specimens needed to be designed.

2.4.2 Definition of the geometry of the representative specimen

A representative specimen is intended to fulfill the thermal history similarity criterion regarding the preheating temperature for a certain ROI of the actual component. In addition, any potential build angle dependency of the resulting properties should be also adopted by the representative specimen. Furthermore, the geometry of the representative specimen needs to have a sufficient size to be used for the preparation of coupons for fatigue testing. Following these requirements, a simple cuboid geometry with a build angle of 45° was chosen as a representative specimen of the cone section of the demonstrator (region A, Fig. 2). The geometry of the representative specimens is shown in Fig. 5.

2.4.3 Development of a strategy to transfer the thermal history of the ROI to the representative specimen

While it can be assumed that the near-temperature field can mainly be transferred using the same laser energy input parameters, an adjustment must be made for the transfer of the geometry-dependend far-temperature field. For this purpose, the ILT was chosen as a variable parameter, which can affect the heat accumulation systematically to achieve the desired preheating temperature level. Figure 6 graphically summerises this strategy. In contrast to an adjustment of the laser energy input parameters, such as laser power or scanning velocity, a variation of the ILT enables the adjustment of the preheating temperature without the need to change defined PBF-LB/M processing parameters. The temperature far field results not only from the ILT, but also from the geometry that has already been built up and its heat dissipation capacity. Since the geometry of the component and the representative specimen changes considerably during the transfer, the ILT appears to be a suitable adjustment variable to compensate this geometric influence. Geometry induced variations of the ILT are common in PBF-LB/M but their impact on the preheating temperature profile is usually neglected, although there is awareness of the influence of the geometrical features on the thermal history, leading to variations in resulting properties of the final part. Only a few PBF-LB/M machines on the market have the option to set so-called minimum exposure times, which can be used to level the ILT to a constant value over the entire course of the production. However, to the authors' knowledge, there

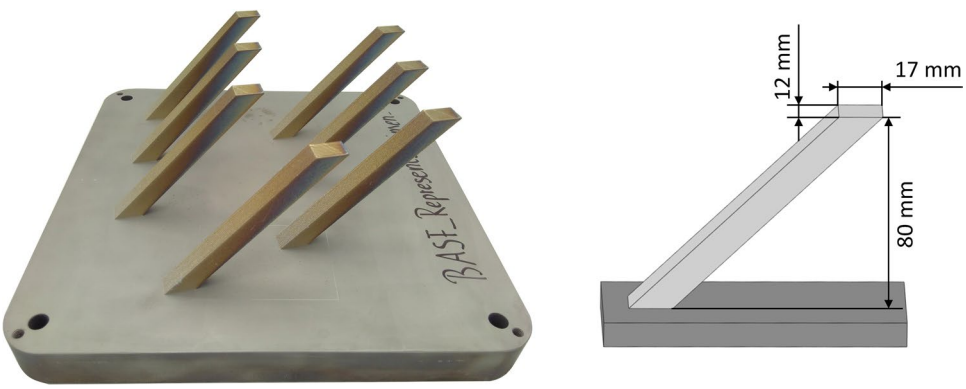

Fig. 5 Representative sample produced by means of PBF-LB/M (left) and CAD geometry (right)

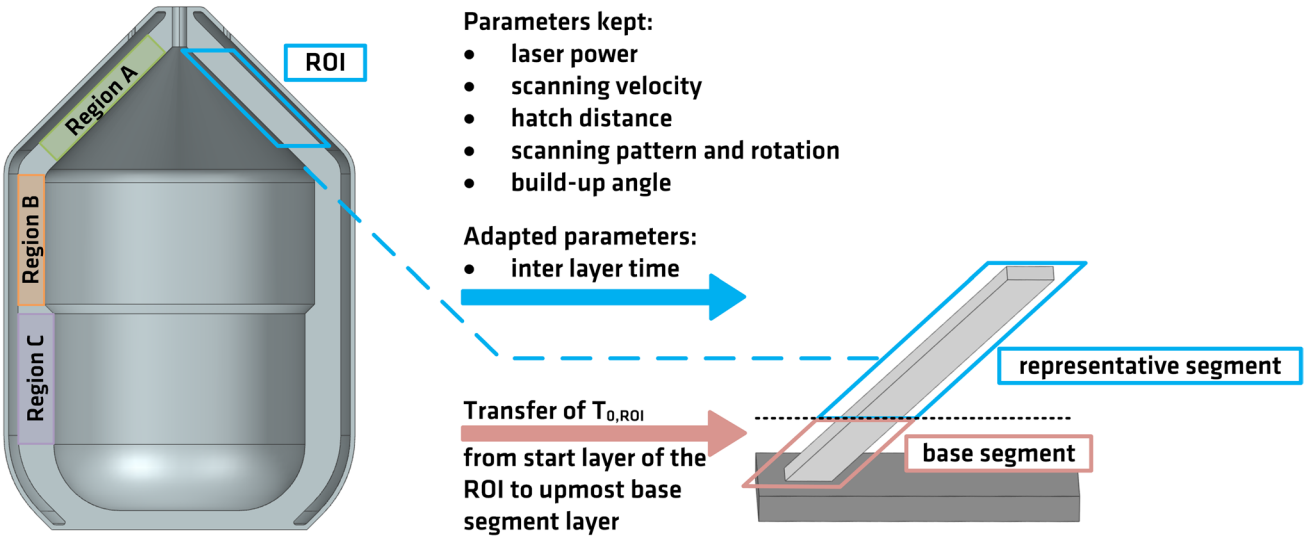

Fig. 6 Schematic illustration of the strategy applied to transfer the thermal history from the demonstrator to the representative specimen

is no machine on the market, which allows for setting a continuously and purposely variable ILT over the course of the layer-wise production. Nonetheless, by designing dummy volumes with changing cross sections, there is the opportunity to implement variations of the ILT independent of the actual parts to be produced. A dummy volume (or ghost part) is defined as a geometrical body, whose laser power is set to 0 W, so that it is scanned but not exposed and, therefore, contributes only to the ILT but does not generate any additional energy input by any laser absorption.

Here, for the first time, such a strategy for the ILT was utilized to achieve predefined preheating temperatures at the top surface of a representative specimen to meet the desired thermal similarity criterion. In other recent work the ILT has also been used as an adjusting parameter not to provoke heat accumulation but rather to avoid heat build-up [9, 23].

The ILT of the component changes between 10 and 100 s (see Fig. 3). In contrast, the x–y-cross-section area of the representative specimens was chosen to be constant over the entire build-up direction (z-direction). This primarily results in a constant ILT of the build process,. However, To ensure thermal similarity, the transfer of the thermal profile succeeded by the integration of a dummy volume with an adequate geometry. The geometry of the dummy part was derived from the modeled ILT requirements and the scanning parameters of the specimens. An iterative process was carried out to define a course of ILT which would result in a similar thermal history for the representative specimens as for the ROI of the vessel using the described macroscale simulation approach.

The lower limit of the ILT was predefined by the cross-section area of the specimens and their number within one build process. The number of specimens was set to seven, resulting in a lower ILT value of 25 s. There was the requirement to reach the initial preheating temperature $T_{0,roi}$ for the ROI at a level of approx. 300 °C (see Fig. 8) within a reasonable manufacturing time and without changes in the geometry of the specimens. This means, that the first 220 layers were manufactured with this constant ILT only to provoke heat accumulation up to the desired temperature level. In this initial heat ramp up phase in the base segment of the specimens, the gradient of the thermal profile of the specimens and the component are allowed to differ completely. Thereafter, the preheating temperature profile of the component needed to be adopted. For this purpose, the ILT was increased. Several ILTs were used in an iterative procedure and their effect on the resultant preheating temperature profile was studied and finally compared to that of the ROI of the original component. The course of the eventually chosen ILT and the resulting geometry of the dummy volume are depicted in Fig. 7. It reached a maximum ILT of approx. 32 s and then decreased for the final layers up to approx. 28.5 s.

3 Results and discussion

A comparison of thermal histories between the demonstrator and the representative specimens is of primary interest to prove the similarity criterion between the ROI of the component and the representative specimen.

3.1 Thermal history of the demonstrator

Figure 8 depicts the preheating temperatures of the inner wall of the pressure vessel over the layer number. The corresponding build height is provided as reference. It contains

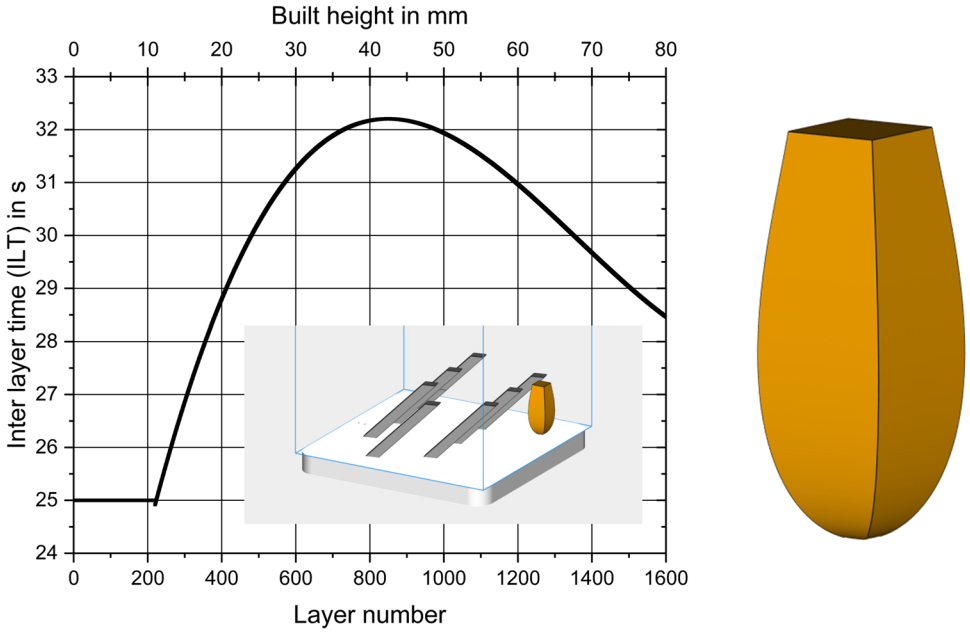

Fig. 7 ILT of the build process of the representative specimen.. The non-constant values are the result of the purposely designed dummy part. The inserted image shows the build-process layout incorporating seven representative specimens (gray) and the dummy part (orange). In addition, the dummy part is displayed enlarged on the right

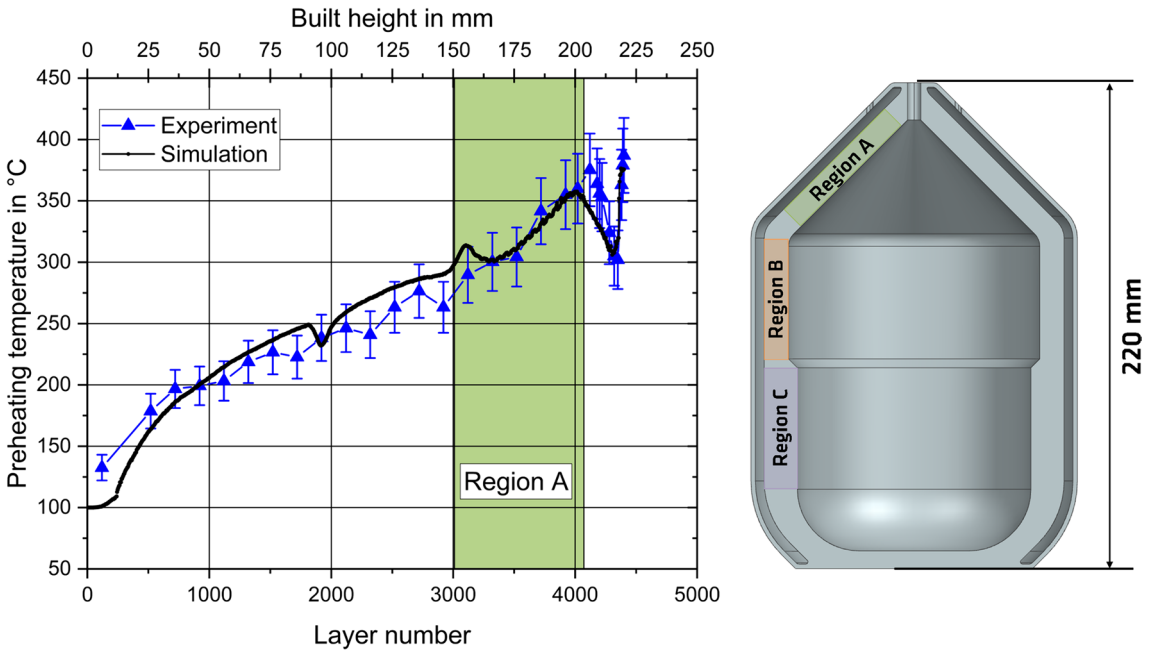

Fig. 8 Comparison between calculated (FEM) and experimental (MWIR) preheating temperature

the results of the FEM simulation as well as the experimentally measured temperatures. In addition, the section of layers of the ROI (region A) is highlighted in green color in the diagram. From the direct comparison of both temperature data sets, a general good agreement between the simulation results and the experimental measurements can be stated, which indicates the validity of the numerical model.

The temperature data indicate a significant deviation of the preheating temperature from the base plate temperature level of 100 °C and also a significant variation throughout the build-up. A global trend of an increase of the preheating temperature with increasing build height can be stated. However, it can also be seen that the curve is non-linear and non-monotonic. This specific trend of

heat accumulation is due to variations of the geometry of the component and the resulting changes in the conditions of heat conduction on the one hand, energy input on the other hand, as well as variation of time for heat dissipation. The experimental finding is quite remarkable since an increase of the preheating temperature to over 350 °C is not to be expected for such a thick-walled structure. According to [24] microstructural changes can already be expected starting from this temperature range.

3.1.1 Comparison of temperature profile and geometry

Up to region C, the heat accumulation increased without interruption. At the transition from region C to B, the thickness of the inner wall of the component decreased from 15 to 11 mm, while the outer wall remained constant. This change in cross-section caused a drop in the temperature curve, as can be seen in the simulation data. The decrease in thickness of the component's wall resulted in comparatively less energy intake per layer. However, the ILT decreased at the same time (cf. Fig. 3), which attenuates this effect and eventually leads to a further increase in the preheating temperature despite the reduced energy intake. The cross-section remained constant for the entire region B, leading to a further increase of the preheating temperature with the growing part. This is comparable to the temperature increase of specimens without geometrical changes over the z-axis, as presented e.g., in [24] and [6].

At the transition from region B to A, the cone starts. The thickness of the inner wall region remained constant, and the wall of the cone is at an angle of 45°. At the curved transition, the energy intake increases as the outer diameter is at a comparable size to the one of region B, but the cross-section to be exposed is increased in the layers of the curved transition. Thereafter, the energy intake per layer decreases constantly with the tapered cone. In addition, the ILT also decreases in that region and finally, the conditions for heat conduction in z-direction are diminished due to the 45° angle. The decreasing ILT and 45° angle overwhelm the effect of reduced energy intake, resulting in a steeper increase in the preheating temperature in region A. Such overhanging structures are known to be regions of heat accumulation [26, 43, 44]. This is due to the reduced thermal conductivity of powder material and solid bulk material as incorporated into the FEM model (see. Figure 4). The lateral heat conduction in z-direction is disturbed in that region.

The sudden decrease of the preheating temperature at the top of region A can be explained by the drastically reduced energy intake due to the smaller cross sections at the layers where the open outlet hole is placed. Eventually, the preheating temperature increases again in the final layers. At very short ILT the inner and outer wall unify and the additional energy intake from the outer wall region contributes to the final temperature increase.

3.2 Numerical modeling of the thermal history of a representative specimen

The red curve in Fig. 9 depicts the resulting simulation outcome of the preheating temperature of the representative specimen. Note, that the temperature profile of the representative specimen was shifted toward the adequate layer numbers to allow a direct comparison with the thermal history of the region A in the demonstrator. The beginning of that temperature curve (prior to layer 3000) was designed to quickly increase the preheating temperature up to a similar level as the beginning of section A in the component. The corresponding part of the test specimen (base segment) should not be used for subsequent determination of mechanical properties and can be used, for example, as a clamping area. It can be seen that the initial thermal gradient is steep. This was achieved by a short ILT of 25 s (see Fig. 7). This short ILT gave the possibility to quickly reach the preheating temperature similar to that of the cone of the demonstrator. It can be seen from Fig. 7 that the ILT increased from 25 s and reached a peak value of approx. 32 s. This increase in ILT allowed more time for heat dissipation for the quickly heated specimen and consequently, the thermal gradient decreased and approximately matched the temperature profile in the region A. For the later layers of the specimen, the ILT decreased again and reached a minimum value of 28.5 s. The transition for the ILT throughout this region is smooth.

Considering the temperature curves in Fig. 9, the choice of the ILT was effective and resulted in good agreement between simulation results for the component and the representative specimen. These results demonstrated that the computational framework could be used for the design of the representative specimens and the choice of the manufacturing parameters.

3.3 Comparison of the thermal similarity between the representative specimen and the ROI of the demonstrator

Figure 10 presents a comparison of the thermal simulation results of the representative specimen and the measured temperature data during the fabrication. In addition, Fig. 11 depicts a comparison of the preheating temperatures measured by thermography on the relevant section of the

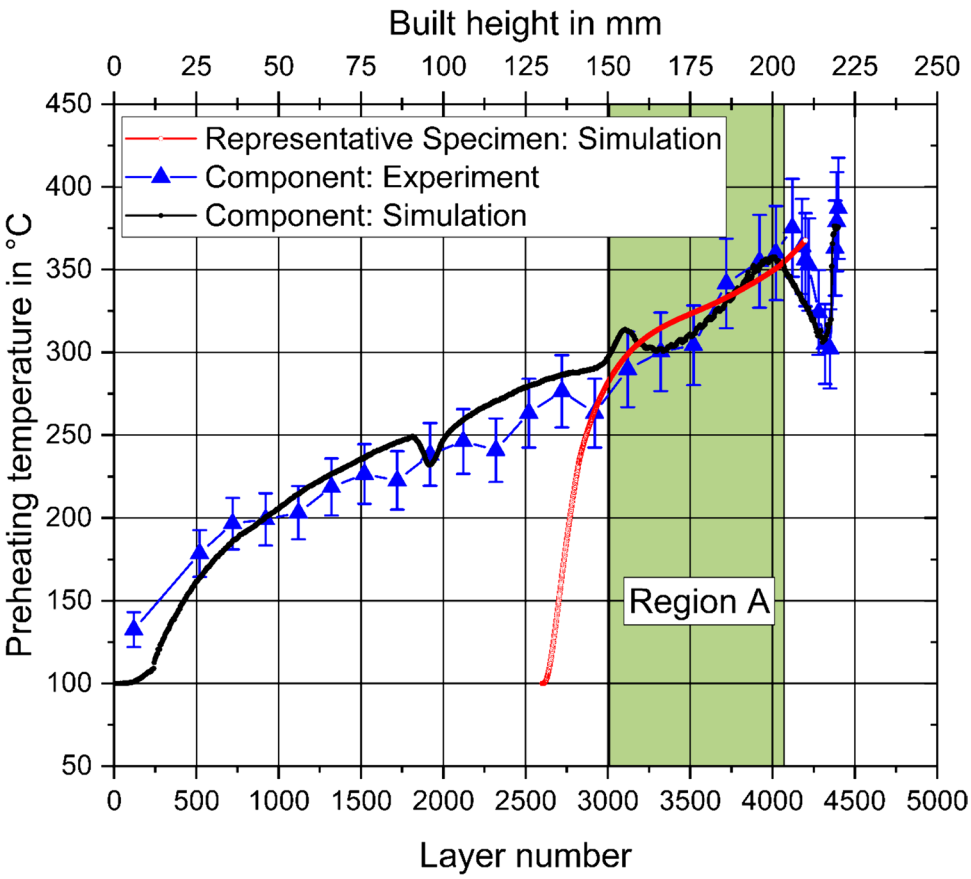

Fig. 9 Comparison of the thermal histories in the demonstrator and in the representative specimen. The simulated temperature for the representative specimen (red line) increases rapidly from the temperature of the base plate (100 °C) over the additional base segment, then it follows with a high degree of approximation the expected temperature over the region of interest"

demonstrator and of the specimen, which represents the ROI. Especially the experimental results show a high degree of similarity in the gradient of the curve as well as in the absolute values of the measured preheating temperature. The preheating temperature of the representative specimen sample starts at 100 °C, which is the temperature of the base plate. Gradually, due to heat accumulation, the specimen's preheating temperature increases, and it converges to the temperature of the component. For the first layers of the ROI, the difference between the component's and specimen's preheating temperature of around 50 °C can be noticed. This discrepancy diminishes in the further course of the build-up and finally, the temperature of the component and the representative specimen are nearly coincident. The deviations at the beginning of the relevant part of the specimens can also be observed in the comparison of the simulation result with the specimen. Further optimization of the model parameters might solve this issue and could provide better ILT predictions which can be used as control parameters.

4 Conclusion

The work presented a new paradigm for the characterization and qualification of parts, namely the use of tailored representative specimens. The key point is to assume that parts and specimens experiencing similar thermal histories are characterized by similar microstructural features and therefore display similar mechanical properties. The possible contribution of the residual stress distribution was not considered in this study.

The implementation of the concept is very straightforward and relies on numerical simulations and thermographic measurements of the thermal histories during the fabrication process. The preheating temperature evolution is taken as a physical quantity based on which the transferability of the thermal history between component and specimen is realized. It was demonstrated that the transferability of the thermal field can be achieved by adjusting the ILT for the fabrication of the specimen to induce a target heat accumulation.

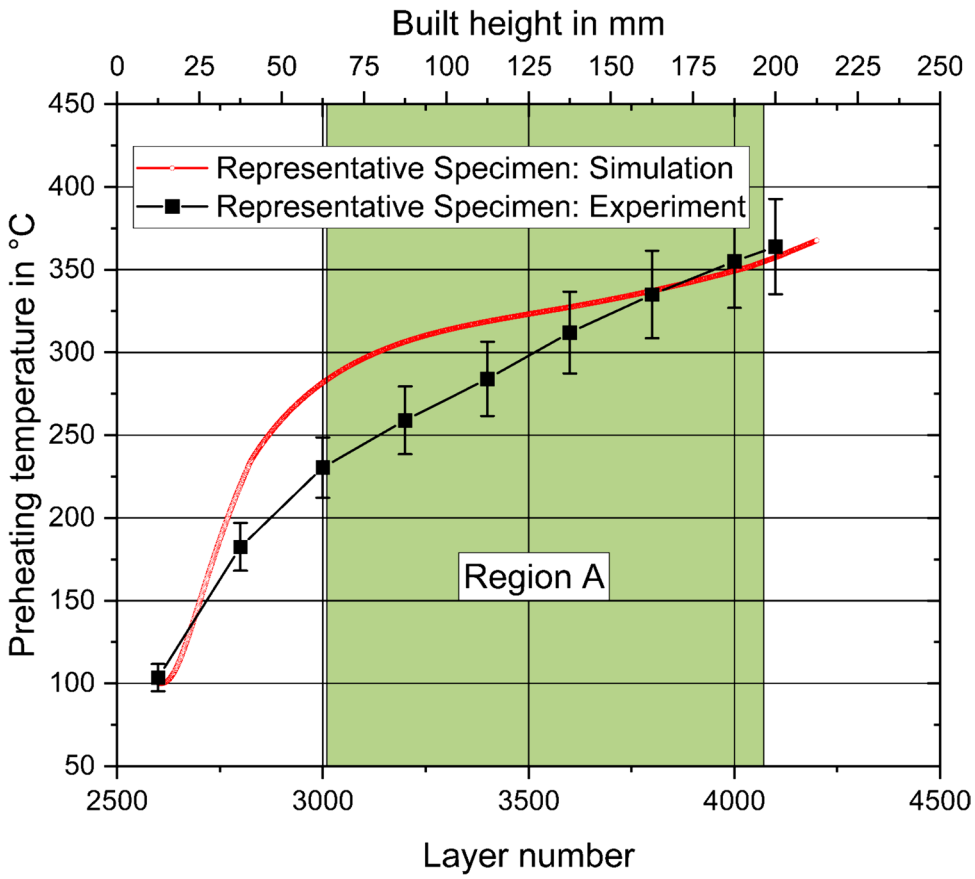

Fig. 10 Thermal history of the representative specimen: Comparison between simulation and experiment

Depsite some deviations between preheating temperatures in the component and in the representative specimens, the general high degree of similarity can be understood as a successful proof of concept for the development of representative specimens. Simulation based on FEM has proven to be a useful tool to design specimens and manufacturing conditions which both can be taken for the manufacturing of simply shaped specimens being representative for a particular ROI of a complex real component in terms of their macroscopic thermal history. Nevertheless, the approach needs to be validated by the comparison of the mechanical and fatigue properties between specimens extracted from the demonstrator and representative specimens. This is the subject of ongoing work.

This strategy can be useful for qualification processes, where instead of manufacturing and testing of whole components, a representative specimen is built. This specimen can then be used for different parametric studies or the investigation of mechanical properties. The FEM-based simulation will provide manufacturing conditions as well as specimen design requirements. The determination of mechanical properties on representative samples that correspond to critical areas in a component, without having to manufacture the component itself, could make future qualification processes significantly faster and more cost-effective.

It must be emphasized that the presented approach of temperature field transfer is only successful if the preheating temperature reached in the component can be achieved by a corresponding adjustment of the ILT in the representative specimens. If thin-walled ROI of components are to be transferred, it may not be possible to achieve the necessary short ILT on the representative specimens, since these may already require a longer ILT due to their cross-sectional area

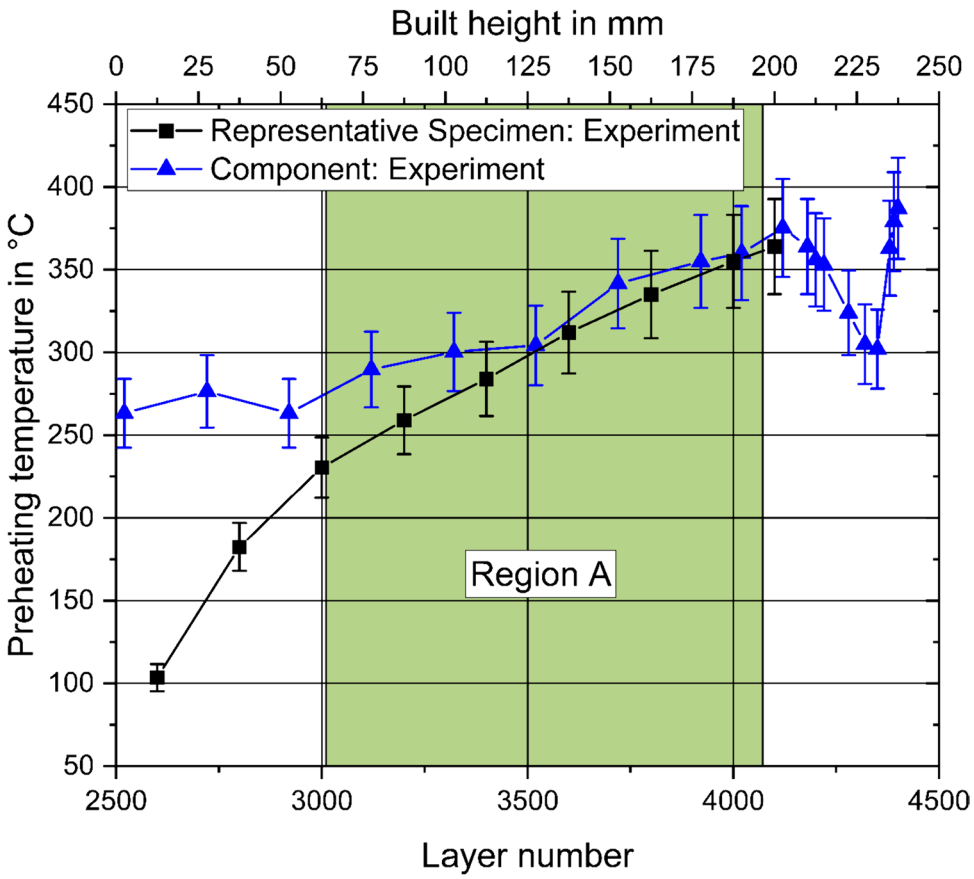

Fig. 11 Thermal history of the ROI of the component and the representative specimen: Comparison between experimentally measured preheating temperatures

and number. This problem can be mitigated using small-scale representative specimens.

Acknowledgements The work presented in this paper is the result of a collaboration between BAM and BASF SE. The authors would like to express their gratitude to Dr. Bernd Glaser from BASF SE for the support and the fruitful discussions.

Author contributions Conceptualization: MC, KH, MM, GM, Data curation: MC, GM, Investigation: MC, GM, NS, Formal analysis: MC, Validation: MC, GM, Visualization: GM, Methodology: MC, GM, Writing—original draft: GM, MC, Writing—review and editing: GM, MC, NS, SG, MM, KH.

Funding Open Access funding enabled and organized by Projekt DEAL.

Data availability Not applicable.

Declarations

Conflict of interest The authors have no conflicts of interest to declare.

References

1. Zerbst U, Bruno G, Buffiere J-Y, Wegener T, Niendorf T, Wu T, Zhang X, Kashaev N, Meneghetti G, Hrabe N, Madia M, Werner T, Hilgenberg K, Koukolíková M, Procházka R, Džugan J, Möller B, Beretta S, Evans A, Wagener R, Schnabel K (2021) Damage tolerant design of additively manufactured metallic components subjected to cyclic loading: state of the art and challenges. Prog Mater Sci 121:100786. https://doi.org/10.1016/j.pmatsci.2021.100786
2. Venturi F, Taylor R (2023) Additive manufacturing in the context of repeatability and reliability. J Mater Eng Perform 32(15):6589–6609. https://doi.org/10.1007/s11665-023-07897-3
3. Sanaei N, Fatemi A, Phan N (2019) Defect characteristics and analysis of their variability in metal L-PBF additive manufacturing. Mater Des 182:108091. https://doi.org/10.1016/j.matdes.2019.108091
4. Mukherjee T, Elmer JW, Wei HL, Lienert TJ, Zhang W, Kou S, DebRoy T (2023) Control of grain structure, phases, and defects in additive manufacturing of high-performance metallic components. Progress Mater Sci. https://doi.org/10.1016/j.pmatsci.2023.101153

5. de Leon Nope GV, Perez-Andrade LI, Corona-Castuera J, Espinosa-Arbelaez DG, Muñoz-Saldaña J, Alvarado-Orozco JM (2021) Study of volumetric energy density limitations on the IN718 mesostructure and microstructure in laser powder bed fusion process. J Manuf Process 64:1261–1272. https://doi.org/10.1016/j.jmapro.2021.02.043
6. Mohr G, Altenburg SJ, Hilgenberg K (2023) On the limitations of small cubes as test coupons for process parameter optimization in laser powder bed fusion of metals. J Laser Appl. https://doi.org/10.2351/7.0001080
7. Mostafaei A, Zhao C, He Y, Ghiaasiaan SR, Shi B, Shao S, Shamsaei N, Wu Z, Kouraytem N, Sun T (2022) Defects and anomalies in powder bed fusion metal additive manufacturing. Curr Opin Solid State Mater Sci 26(2):100974. https://doi.org/10.1016/j.cossms.2021.100974
8. Nahr F, Rasch M, Burkhardt C, Renner J, Baumgärtner B, Hausotte T, Körner C, Steinmann P, Mergheim J, Schmidt M, Markl M (2023) Geometrical influence on material properties for Ti6Al4V parts in powder bed fusion. J Manuf Mater Process. https://doi.org/10.3390/jmmp7030082
9. Koenis TPA, Montero-Sistiaga ML, De Smit MJ, Amsterdam E (2023) Simulation-based process optimization towards homogeneous Ti6Al4V L-PBF components. In: Proceedings of IVth International Conference on simulation for additive manufacturing (Sim-AM 2023), Munich, Germany
10. Yavari R, Smoqi Z, Riensche A, Bevans B, Kobir H, Mendoza H, Song H, Cole K, Rao P (2021) Part-scale thermal simulation of laser powder bed fusion using graph theory: effect of thermal history on porosity, microstructure evolution, and recoater crash. Mater Des 204:109685. https://doi.org/10.1016/j.matdes.2021.109685
11. Chandrasekar S, Coble JB, List F, Carver K, Beauchamp S, Godfrey A, Paquit V, Babu SS (2022) Similarity analysis for thermal signature comparison in metal additive manufacturing. Mater Des. https://doi.org/10.1016/j.matdes.2022.111261
12. Munk J, Breitbarth E, Siemer T, Pirch N, Häfner C (2022) Geometry effect on microstructure and mechanical properties in laser powder bed fusion of Ti-6Al-4V. Metals. https://doi.org/10.3390/met12030482
13. DebRoy T, Wei HL, Zuback JS, Mukherjee T, Elmer JW, Milewski JO, Beese AM, Wilson-Heid A, De A, Zhang W (2018) Additive manufacturing of metallic components—process, structure and properties. Prog Mater Sci 92:112–224. https://doi.org/10.1016/j.pmatsci.2017.10.001
14. Kok Y, Tan XP, Wang P, Nai MLS, Loh NH, Liu E, Tor SB (2018) Anisotropy and heterogeneity of microstructure and mechanical properties in metal additive manufacturing: a critical review. Mater Des 139:565–586. https://doi.org/10.1016/j.matdes.2017.11.021
15. Charmi A, Falkenberg R, Ávila L, Mohr G, Sommer K, Ulbricht A, Sprengel M, Saliwan Neumann R, Skrotzki B, Evans A (2021) Mechanical anisotropy of additively manufactured stainless steel 316L: an experimental and numerical study. Mater Sci Eng, A 799:140154. https://doi.org/10.1016/j.msea.2020.140154
16. Rehmer B, Bayram F, Avila Calderon LA, Mohr G, Skrotzki B (2023) Elastic modulus data for additively and conventionally manufactured variants of Ti-6Al-4V, IN718 and AISI 316 L. Sci Data 10(1):474. https://doi.org/10.1038/s41597-023-02387-6
17. Vaneker T, Bernard A, Moroni G, Gibson I, Zhang Y (2020) Design for additive manufacturing: framework and methodology. CIRP Ann 69(2):578–599. https://doi.org/10.1016/j.cirp.2020.05.006
18. Mohr G, Altenburg SJ, Hilgenberg K (2020) Effects of inter layer time and build height on resulting properties of 316L stainless steel processed by laser powder bed fusion. Addit Manuf 32:101080. https://doi.org/10.1016/j.addma.2020.101080
19. Williams RJ, Piglione A, Rønneberg T, Jones C, Pham M-S, Davies CM, Hooper PA (2019) In situ thermography for laser powder bed fusion: effects of layer temperature on porosity, microstructure and mechanical properties. Addit Manuf 30:100880. https://doi.org/10.1016/j.addma.2019.100880
20. Mohr G, Scheuschner N, Hilgenberg K (2020) In situ heat accumulation by geometrical features obstructing heat flux and by reduced inter layer times in laser powder bed fusion of AISI 316L stainless steel. CIRP Proc 94:155–160. https://doi.org/10.1016/j.procir.2020.09.030
21 Ranjan R, Ayas C, Langelaar M, van Keulen F (2020) Fast detection of heat accumulation in powder bed fusion using computationally efficient thermal models. Materials 13(20):10. https://doi.org/10.3390/ma13204576
22. Ranjan R, Chen Z, Ayas C, Langelaar M, Van Keulen F (2023) Overheating control in additive manufacturing using a 3D topology optimization method and experimental validation. Addit Manuf 61:10. https://doi.org/10.1016/j.addma.2022.103339
23. Riensche A, Bevans BD, Smoqi Z, Yavari R, Krishnan A, Gilligan J, Piercy N, Cole K, Rao P (2022) Feedforward control of thermal history in laser powder bed fusion: toward physics-based optimization of processing parameters. Mater Des. https://doi.org/10.1016/j.matdes.2022.111351
24. Mohr G, Sommer K, Knobloch T, Altenburg SJ, Recknagel S, Bettge D, Hilgenberg K (2021) Process induced preheating in laser powder bed fusion monitored by thermography and its influence on the microstructure of 316L stainless steel parts. Metals 11(7):1063. https://doi.org/10.3390/met11071063
25. Pauzon C, Dietrich K, Forêt P, Hryha E, Witt G (2021) Mitigating oxygen pick-up during laser powder bed fusion of Ti-6Al-4V by limiting heat accumulation. Mater Lett 288:129365. https://doi.org/10.1016/j.matlet.2021.129365
26. Zielinski J, Theunissen J, Kruse H, Rittinghaus S-K, Schleifenbaum JH, Zhu D, Megahed M (2023) Understanding inhomogeneous mechanical properties in PBF-LB/M manufactured parts due to inhomogeneous macro temperature profiles based on process-inherent preheating. J Manuf Mater Process 7(3):10. https://doi.org/10.3390/jmmp7030088
27. Zerbst U, Madia M, Bruno G, Hilgenberg K (2021) Towards a methodology for component design of metallic AM parts subjected to cyclic loading. Metals 11(5):709. https://doi.org/10.3390/met11050709
28. Pantawane MV, Ho YH, Joshi SS, Dahotre NB (2020) Computational assessment of thermokinetics and associated microstructural evolution in laser powder bed fusion manufacturing of Ti6Al4V alloy. Sci Rep 10(1):7579. https://doi.org/10.1038/s41598-020-63281-4
29. Kelly S, Kampe S (2004) Microstructural evolution in laser-deposited multilayer Ti-6Al-4V builds: part I. Microstructural characterization. Metallur Mater Trans A 35:1861–1867
30. Paulson NH, Gould B, Wolff SJ, Stan M, Greco AC (2020) Correlations between thermal history and keyhole porosity in laser powder bed fusion. Addit Manuf. https://doi.org/10.1016/j.addma.2020.101213
31. Räpke T, Heinze C, Hilgenberg K, Hongwu X, Scheuschner N, Mühlenweg A, Obadasi E, Rule D, Hayduk M (2022) Geometrie- und Prozesseinflüsse auf lokale Bauteileigenschaften in der metallischen additiven Fertigung mittels Laserstrahlschmelzen. 3. Fachtagung Werkstoffe und Additive Fertigung 2022, Dresden, Germany
32. Mohr G, Nowakowski S, Altenburg SJ, Maierhofer C, Hilgenberg K (2020) Experimental determination of the emissivity of powder layers and bulk material in laser powder bed fusion using infrared

thermography and thermocouples. Metals 10(11):1546–1557. https://doi.org/10.3390/met10111546
33. Chaudry MA, Mohr G, Hilgenberg K (2022) Experimental and numerical comparison of heat accumulation during laser powder bed fusion of 316L stainless steel. Progress Addit Manuf. https://doi.org/10.1007/s40964-022-00282-x
34. Hughes TJ (2012) The finite element method: linear static and dynamic finite element analysis. Courier Corporation
35. King WE, Barth HD, Castillo VM, Gallegos GF, Gibbs JW, Hahn DE, Kamath C, Rubenchik AM (2014) Observation of keyhole-mode laser melting in laser powder-bed fusion additive manufacturing. J Mater Process Technol 214(12):2915–2925. https://doi.org/10.1016/j.jmatprotec.2014.06.005
36. Trapp J, Rubenchik AM, Guss G, Matthews MJ (2017) In situ absorptivity measurements of metallic powders during laser powder-bed fusion additive manufacturing. Appl Mater Today 9:341–349. https://doi.org/10.1016/j.apmt.2017.08.006
37. Fabbro R, Chouf K (2000) Keyhole modeling during laser welding. J Appl Phys 87(9):4075–4083. https://doi.org/10.1063/1.373033
38. Seidel C, Zaeh MF (2018) Multi-scale modelling approach for contributing to reduced distortion in parts made by laser-based powder bed fusion. Proc CIRP 67:197–202. https://doi.org/10.1016/j.procir.2017.12.199
39. Khan K, Mohr G, Hilgenberg K, De A (2020) Probing a novel heat source model and adaptive remeshing technique to simulate laser powder bed fusion with experimental validation. Comput Mater Sci 181:109752. https://doi.org/10.1016/j.commatsci.2020.109752
40. Ulbricht A, Mohr G, Altenburg SJ, Oster S, Maierhofer C, Bruno G (2021) Can potential defects in LPBF be healed from the laser exposure of subsequent layers? A quantitative study. Metals 11(7):1012–1026. https://doi.org/10.3390/met11071012
41. Mills KC (2002) Recommended values of thermophysical properties for selected commercial alloys. Woodhead Publishing, Cambridge
42. Sih SS, Barlow JA (1995) The prediction of the thermal conductivity of powders. In: International Solid Freeform Fabrication Symposium, Austin, TX, USA
43. Han Q, Gu H, Soe S, Setchi R, Lacan F, Hill J (2018) Manufacturability of AlSi10Mg overhang structures fabricated by laser powder bed fusion. Mater Des 160:1080–1095. https://doi.org/10.1016/j.matdes.2018.10.043
44. Ilin A, Logvinov R, Kulikov A, Prihodovsky A, Xu H, Ploshikhin V, Günther B, Bechmann F (2014) Computer aided optimisation of the thermal management during laser beam melting process. Phys Proc 56:390–399. https://doi.org/10.1016/j.phpro.2014.08.142